

# Introducing GPU-acceleration into the Python-based Simulations of Chemistry Framework

Rui Li,<sup>1</sup> Qiming Sun,<sup>2</sup> Xing Zhang,<sup>1</sup> and Garnet Kin-Lic Chan<sup>1, a)</sup>

<sup>1)</sup> *Division of Chemistry and Chemical Engineering, California Institute of Technology*

<sup>2)</sup> *Quantum Engine LLC.*

We introduce the first version of GPU4PySCF, a module that provides GPU acceleration of methods in PySCF. As a core functionality, this provides a GPU implementation of two-electron repulsion integrals (ERIs) for contracted basis sets comprising up to  $g$  functions using Rys quadrature. As an illustration of how this can accelerate a quantum chemistry workflow, we describe how to use the ERIs efficiently in the integral-direct Hartree-Fock Fock build and nuclear gradient construction. Benchmark calculations show a significant speedup of two orders of magnitude with respect to the multi-threaded CPU Hartree-Fock code of PySCF, and performance comparable to other GPU-accelerated quantum chemical packages including GAMESS and QUICK on a single NVIDIA A100 GPU.

## I. INTRODUCTION

The rapid advances in the capabilities of graphics processing units (GPUs) has significantly impacted many fields, including graphics rendering, gaming, and artificial intelligence.<sup>1,2</sup> The massively parallel architecture of GPUs offers drastically more computational throughput than traditional central processing units (CPUs), making them well-suited for computationally intensive tasks such as dense matrix multiplication and tensor contraction.<sup>3</sup> Consequently, GPUs have evolved into powerful tools for scientific computation on high-performance computing (HPC) platforms. For instance, at the National Energy Research Scientific Computing Center, GPUs deliver a maximum compute performance of 119.8 PFLOPS compared to only 11.6 PFLOPS from the associated CPUs.<sup>4</sup> However, leveraging GPUs for substantial performance gains over CPUs typically requires significant redesign of algorithms.

In the field of quantum chemistry, GPUs have been extensively explored to accelerate the Hartree-Fock (HF) and density functional theory (DFT) methods. Particular attention has been paid to evaluating two-electron repulsion integrals (ERIs), a key computational primitive, and their subsequent use in the Fock builds of the HF and DFT equations. Over the past 15 years, various GPU algorithms for ERI evaluation and the Fock builds have been proposed. Yasuda<sup>5</sup> implemented the first such algorithm, along with the construction of the Coulomb matrix using the J engine method.<sup>6,7</sup> At the same time, Ufimtsev and Martínez<sup>8,9</sup> developed a GPU implementation for the HF method, which included building the full Fock matrix (both Coulomb and exchange matrices), with ERIs evaluated using the McMurchie-Davidson (MD) algorithm.<sup>10</sup> Both implementations were initially limited to Gaussian basis sets containing only  $s$  and  $p$  functions. Later, Asadchev and Gordon<sup>11</sup> developed a Fock build algorithm using the Rys quadrature

method<sup>12,13</sup> for ERI evaluation, allowing for the use of uncontracted basis sets with up to  $g$  functions. In addition, Miao and Merz<sup>14</sup> employed the Head-Gordon-Pople (HGP) algorithm<sup>15</sup> to reduce the number of floating-point operations (FLOPs) required for computing ERIs with contracted basis functions. Recently, Barca *et al.* introduced a distinct implementation of the HGP algorithm and an improved ERI digestion (the contraction between ERIs and the density matrix to form the Fock matrix) scheme.<sup>16</sup> This was subsequently extended to run on multiple GPUs.<sup>17,18</sup> Their code outperformed most previous multi-GPU implementations, but significant performance drops were observed for ERIs involving basis functions with higher angular momenta, such as  $d$  functions. To address this issue, Asadchev and Valeev<sup>19,20</sup> developed a matrix-based formulation of the MD algorithm, leveraging extensive use of dense matrix multiplication kernels. Their approach achieved significant speedups over the reference CPU implementation, particularly for high angular momentum ERIs, including those involving  $i$  functions.

In this work, we describe our implementation of four-center ERIs on the GPU within the GPU4PySCF module. As a core computational routine, this was the first feature to be developed. At the time of writing, GPU4PySCF also contains many additional features, including those developed using GPU-accelerated density fitting ERIs<sup>21</sup> (which are computed using an adaptation of the four-center ERI algorithm). However, to limit the scope of this paper to the work of the current set of authors, as well as to present the chronological development of the package, this work describes only the algorithm for four-center ERIs and the subsequent Fock build routines that use them.

Our ERI implementation is based on Rys quadrature. One advantage of this technique is that it features a small memory footprint, making it well-suited for mainstream commodity GPUs with limited fast on-chip memory. Additionally, it offers simple recurrence relations, facilitating straightforward extensions to high angular momentum and ERI derivatives. Within this framework, we utilize several algorithmic optimizations to enhance the per-

<sup>a)</sup> Electronic mail: gkc1000@gmail.com

formance of both energy and nuclear gradient ERI evaluation with the latest compute unified device architecture (CUDA). The resulting ERI routines support contracted basis sets comprising up to  $g$  functions.

GPU4PySCF is designed to operate primarily within the Python environment. Consequently, in addition to the custom CUDA kernels for the ERIs, it utilizes NUMPY<sup>22</sup>-like packages (such as CUPY<sup>23</sup>) to accelerate the computationally expensive tensor contractions and linear algebra operations on the GPU. The Python-based nature of GPU4PySCF allows for seamless integration with other Python-based workflows, particularly those in machine learning applications. We envision that this choice of ecosystem for quantum chemistry GPU acceleration will allow GPU4PySCF to achieve the same type of interdisciplinary impact that its parent package PySCF has become known for.<sup>24</sup>

The paper is organized as follows. Section II provides a brief review of the Rys quadrature method. Sections III and IV detail our GPU-accelerated Hartree-Fock (HF) implementation, focusing on the algorithms for Fock build and nuclear gradients, respectively. The performance of our method is examined in Section V. Finally, we draw some conclusions and describe our general outlook for GPU4PySCF in Section VI.

## II. RYS QUADRATURE METHOD

In the Rys quadrature method,<sup>12,13,25</sup> the six-dimensional ERI is expressed as a product of three two-dimensional (2D) integrals ( $I_x$ ,  $I_y$ , and  $I_z$ ), evaluated exactly by an  $N$ -point Gaussian quadrature with weights ( $w_n$ ) and roots ( $t_n$ ) of the Rys polynomial:

$$[ab|cd] = \sum_n^N w_n I_x(t_n) I_y(t_n) I_z(t_n). \quad (1)$$

In Eq. (1), the ERI is computed for Cartesian primitive Gaussian functions (PGFs),

$$|a] \equiv \phi_a(\mathbf{r}) = (x - A_x)^{a_x} (y - A_y)^{a_y} (z - A_z)^{a_z} e^{-\alpha|\mathbf{r}-\mathbf{A}|^2}, \quad (2)$$

which are centered at nuclear positions  $\mathbf{A} = (A_x, A_y, A_z)$ , with exponents  $\alpha$  and angular momenta  $a = a_x + a_y + a_z$ . The number of quadrature points is related to the angular momenta of the four PGFs as

$$N = \left\lfloor \frac{a + b + c + d}{2} \right\rfloor + 1. \quad (3)$$

The 2D integrals  $I_x$ ,  $I_y$ , and  $I_z$  are evaluated for each primitive shell quartet (denoted as  $[\mathbf{ab}|\mathbf{cd}]$ , where bold letters indicate a shell of basis functions), using the recurrence and transfer relations (RRs).<sup>12,13</sup> Each of the 2D integral tensors has a size of  $(a+1)(b+1)(c+1)(d+1)$  for each quadrature point. Finally, for contracted Gaussian functions (CGFs), which are linear combinations (with

contraction order  $K$ ) of PGFs,

$$|i] = \sum_a^K C_a^i |a], \quad (4)$$

the contracted ERI can be written as

$$(ij|kl) = \sum_{abcd} C_a^i C_b^j C_c^k C_d^l [ab|cd]. \quad (5)$$

Modern GPUs offer high computational throughput but often suffer from significant memory latency. They are well-suited for tasks with high arithmetic intensity [defined as the ratio of FLOPs to data movement (in bytes)], such as dense matrix multiplications, where the latency can be effectively masked. ERI evaluation using the Rys quadrature method may or may not fall into this category of tasks depending on the feasibility of data caching in fast memory. We can roughly estimate its arithmetic intensity by considering the most computationally expensive step, i.e., Eq. (1). If no data is cached, the arithmetic intensity is approximately  $\frac{3}{16}$  FLOP/byte. This intensity is significantly below the peak FLOP rate to memory bandwidth ratio of  $\frac{9.7\text{TFLOP/s}}{1.6\text{TB/s}} = 6.1\text{FLOP/byte}$  for the NVIDIA A100 GPU used in this work. According to the Roofline model,<sup>26</sup> it suggests that the corresponding implementation will be memory-bound and likely inefficient. On the other hand, if the ERIs and 2D integrals can be cached completely, the arithmetic intensity becomes  $\frac{3NK}{8}$  FLOP/byte (assuming we are storing the results in slow memory). This value can be higher than the previous ratio for large  $N$  and  $K$ , indicating a compute-bound character. However, GPUs typically have limited fast memory (e.g., registers and shared memory), and hence require careful algorithmic design to achieve optimal performance.

The Rys quadrature method features a low memory footprint<sup>11</sup> and high data locality,<sup>27</sup> which allows for more effective data caching. For instance, to compute ERIs with  $N \leq 3$ , the necessary data can almost entirely fit into the registers. Specifically, for the integral class (**pp|pp**), the required intermediates (only considering the contracted ERIs and 2D integrals) amount to  $3^4 + 3 \times 2^4 = 129$  FP64 words (equivalent to 258 FP32 words). This is just above the maximum register file size allowed for an NVIDIA GPU thread, which is 255 FP32 words (for the microarchitectures since Kepler). However, for larger  $N$  values, the data size will inevitably exceed the available resources of fast memory. As a result, the implementation must minimize access to slow memory (e.g., local and global memory). In practice, we incorporate the following designs:

1. For ERIs with small  $N$  values, the RRs are unrolled to fully utilize registers.
2. In general cases, we perform ERI digestion before contraction and introduce novel intermediates to minimize global memory access.

- When computing the nuclear gradients, double contractions between the ERI gradients and the density matrix are performed to directly obtain the energy gradients, thereby avoiding the need to store the Fock matrix gradients.

These are detailed in Secs. III and IV.

### III. FOCK BUILD

Algorithm 1 illustrates the workflow for building the Fock matrix. (The actual implementation incorporates vectorization and accounts for the eight-fold permutation symmetry of the ERIs.) Strategies similar to those employed by Barca *et al.*<sup>16</sup> are used for integral screening and workload partitioning. The algorithm starts by grouping the shells of CGFs that share the same angular momentum and contraction order, forming sets of shells denoted as  $|\mathbf{a}, K_a\rangle$  (line 1). Shell pairs are then constructed using Cartesian products between the shells in each group, resulting in  $|\mathbf{ab}, K_a K_b\rangle = |\mathbf{a}, K_a\rangle \otimes |\mathbf{b}, K_b\rangle$  (line 6). These pairs are further “binned” into  $n_{\mathbf{ab}}$  batches indexed by the size parameter  $s_{\mathbf{ab}}$  (line 8), defined as

$$s_{\mathbf{ab}} = \begin{cases} \left\lfloor \frac{\log_{10} I_{\mathbf{ab}}}{\log_{10} \tau} n_{\mathbf{ab}} \right\rfloor, & I_{\mathbf{ab}} < 1 \\ 0, & I_{\mathbf{ab}} \geq 1 \end{cases}, \quad (6)$$

where the labels for contraction orders are omitted for clarity (similarly hereafter). In Eq. (6),  $\tau$  is a positive integral accuracy threshold smaller than one,  $n_{\mathbf{ab}}$  is a heuristic parameter determined such that each bin contains roughly 128 shell pairs, and

$$I_{\mathbf{ab}} = \max_{a \in \mathbf{a}, b \in \mathbf{b}} |(ab|ab)|^{\frac{1}{2}} \quad (7)$$

is the conventional Cauchy-Schwarz bound factor.<sup>28</sup> Note that the shell pairs are prescreened based on the condition  $I_{\mathbf{ab}} > \tau$  before the binning process (line 7), ensuring that at most  $n_{\mathbf{ab}}$  bins are generated.

The main computational loops are executed over the sets of “bra-ket” shell quartets, namely,  $\{\mathbf{ab}|\mathbf{cd}\} = \{\mathbf{ab}\} \otimes \{\mathbf{cd}\}$  (lines 10–11). For each set, a loop over the  $n_{\mathbf{cd}}$  batches of the ket shell pairs is further carried out (line 12), within which the significant bra shell pairs are selected according to the criterion  $I_{|\mathbf{ab}\rangle} I_{|\mathbf{cd}\rangle} P_{\{\mathbf{ab}|\mathbf{cd}\}} > \tau$  (line 14), where

$$I_{|\mathbf{ab}\rangle} = \max_{a \in |\mathbf{a}\rangle, b \in |\mathbf{b}\rangle} I_{\mathbf{ab}}, \quad (8)$$

and

$$P_{\{\mathbf{ab}|\mathbf{cd}\}} = \max_{\substack{i, j \in \{\mathbf{a}, \mathbf{b}, \mathbf{c}, \mathbf{d}\} \\ i \neq j}} |P_{\{i|j\}}| \quad (9)$$

is the maximum element across the corresponding sub-blocks of the density matrix (e.g.,  $P_{\{\mathbf{a}|\mathbf{b}\}}$  represents the

blocks with bra and ket basis functions belonging to  $|\mathbf{a}\rangle$  and  $|\mathbf{b}\rangle$  shell batches, respectively). This screening procedure is performed at the level of batches of shell pairs, which preserves the continuous layout of the shell pair data and facilitates efficient coalesced memory access by the GPU threads. Finally, the GPU kernel (`jk_kernel`) is dispatched to compute the Coulomb ( $\mathbf{J}$ ) and exchange ( $\mathbf{K}$ ) matrices using the screened shell quartets (line 16).

---

#### Algorithm 1. Workflow of building the Fock matrix

---

```

1 shl_sets = [|\mathbf{a}\rangle, |\mathbf{b}\rangle, \dots]
2 shlpr_sets = []
3 for |\mathbf{a}\rangle in shl_sets:
4     for |\mathbf{b}\rangle in shl_sets:
5         |\mathbf{ab}\rangle = [|\mathbf{a}\rangle, |\mathbf{b}\rangle] * n_ab
6         for |\mathbf{ab}\rangle in |\mathbf{a}\rangle \otimes |\mathbf{b}\rangle:
7             if I_ab > \tau:
8                 |\mathbf{ab}\rangle[s_ab].append(|\mathbf{ab}\rangle)
9                 shlpr_sets.append(|\mathbf{ab}\rangle)
10 for |\mathbf{ab}\rangle in shlpr_sets:
11     for |\mathbf{cd}\rangle in shlpr_sets:
12         for s_cd in range(n_cd):
13             for s_ab in range(n_ab):
14                 if I_|\mathbf{ab}\rangle[s_ab] I_|\mathbf{cd}\rangle[s_cd] P_{|\mathbf{ab}|\mathbf{cd}\rangle} < \tau:
15                     break
16     jk_kernel(|\mathbf{ab}\rangle[:s_ab] \otimes |\mathbf{cd}\rangle[s_cd]) #on GPU

```

---

The Fock build is parallelized over a 2D GPU thread grid, with the bra shell pairs distributed in one dimension and the ket shell pairs in the other. Each thread evaluates the ERIs of a shell quartet, contracts them with the density matrix, and accumulates the results into the  $\mathbf{J}/\mathbf{K}$  matrix. Workload balance among the threads is ensured given that the shell quartets are of the same type (with respect to angular momenta and contraction orders).

As mentioned in Section II, the GPU kernel `jk_kernel` has two distinct designs depending on the value of  $N$ . For  $N \leq 3$  (see Algorithm 2), we use metaprogramming to unroll the loops involved in the evaluation of the RRs (line 6), thereby explicitly storing the 2D integrals ( $I_x$ ,  $I_y$ , and  $I_z$ ) and other intermediates in registers to minimize the memory latency. In addition, the primitive ERIs are first contracted (line 7) before being digested (lines 8–13), as sufficient registers are available to hold the contracted ERIs. (Note that the contraction coefficients and the Rys quadrature weights have been absorbed into  $I_x$ ,  $I_y$ , and  $I_z$  in Algorithm 2.) Similarly, loops associated with the ERI digestion are also unrolled, with the final results accumulated into the  $\mathbf{J}/\mathbf{K}$  matrix (stored in global memory) using the atomic operation (`atomicAdd`), which avoids explicit thread synchronizations.

For larger  $N$  values, `jk_kernel` adopts a general implementation, where the key difference is that the ERI digestion now occurs before the contraction. This can be seen from Algorithm 3 that the  $\mathbf{J}/\mathbf{K}$  matrix is updated (e.g., line 23) within the loops over the basis func-

**Algorithm 2.** jk kernel for  $N \leq 3$ 


---

```

1 (ab|cd) = 0
2 for |ab| in |ab|:
3   for |cd| in |cd|:
4     t, w = rys_roots<N>() #Rys roots/weights
5     for i in range(N):
6       Ix, Iy, Iz = rr<N>(t[i], w[i]) #unroll RRs
7       (ab|cd) += Ix * Iy * Iz

#For each element of J/K:
8 atomicAdd(Jab, (ab|cd) * Pcd)
9 atomicAdd(Jcd, (ab|cd) * Pab)
10 atomicAdd(Kac, (ab|cd) * Pbd)
11 atomicAdd(Kbd, (ab|cd) * Pac)
12 atomicAdd(Kad, (ab|cd) * Pbc)
13 atomicAdd(Kbc, (ab|cd) * Pad)

```

---

tions. Because the contracted ERIs no longer fit into registers or fast memory, the contraction-then-digestion procedure will result in storing to and loading from global memory, which may significantly hinder the performance. Due to the same reason, the 2D integrals can only be stored in local memory. They are computed once for all the Rys roots (line 5) to avoid increasing the number of updates to the **J/K** matrix. Furthermore, to reduce global memory loads for retrieving the density matrix, reusable strides (i.e.,  $P_{ac}$  and  $P_{ad}$ ) are cached in local memory, potentially benefiting from optimal L1 and L2 cache utilization. The same strategy applies to temporary stores of the potential matrix (i.e.,  $V_{ac}$  and  $V_{ad}$ ). Additional scalar intermediates are also introduced (e.g.,  $P_{cd}$  and  $V_{cd}$ ), which use registers for data loads and stores. While shared memory (part of the L1 cache) could be used for data caching, our experiment showed that it did not lead to better performance. Since the cached intermediates are streaming rather than persistent data, the compiler may optimize their memory usage more effectively than through manual manipulation.

Finally, it should be noted that the demand for local memory in Algorithm 3 increases rapidly with the rise in angular momentum. For example, the integral class of (ii|ii) requires 731 KB of storage for the 2D integrals, which exceeds the maximum allowed local memory of 512 KB per thread on the NVIDIA A100 GPU used here. Therefore, our present implementation only supports ERIs with up to  $g$  functions.

#### IV. NUCLEAR GRADIENT

The nuclear gradient of the electronic energy in the Hartree-Fock method is expressed as

$$\nabla_{\mathbf{R}} E = \nabla_{\mathbf{R}} (E_{\text{core}} + E_J + E_K) - \sum_{ab} W_{ab} \nabla_{\mathbf{R}} S_{ab}, \quad (10)$$

where  $E_{\text{core}}$  represents the energy associated with the one-electron core Hamiltonian,  $E_J$  and  $E_K$  denote the

**Algorithm 3.** jk kernel for  $N > 3$ 


---

```

1 get idx[...] #precomputed ERI to Ix, Iy, Iz mapping
2 for |ab| in |ab|:
3   for |cd| in |cd|:
4     t, w = rys_roots<N>() #Rys roots/weights
5     Ix, Iy, Iz = rr<N>(t, w) #RRs for all roots
6     #15 is the size of a g shell
7     allocate Vac[15], Vad[15], Pac[15], Pad[15]
8     for |d| in |d|:
9       Vad[...] = 0
10      Pad[...] = P(a|d)
11      for |c| in |c|:
12        Vac[...] = Vcd = 0
13        Pac[...] = P(a|c)
14        Pcd = Pcd
15        for |b| in |b|:
16          Vbc = Vbd = 0
17          Pbc = Pbc
18          Pbd = Pbd
19          for |a| in |a|:
20            α, β, γ = idx[a, b, c, d]
21            g = 0
22            for i in range(N):
23              g += Ix[i, α] * Iy[i, β] * Iz[i, γ]
24            atomicAdd(Jab, g * Pcd)
25            Vac[a] += g * Pbd
26            Vad[a] += g * Pbc
27            Vbc += g * Pad[a]
28            Vbd += g * Pac[a]
29            Vcd += g * Pab
30            atomicAdd(Kbc, Vbc)
31            atomicAdd(Kbd, Vbd)
32          for |a| in |a|:
33            atomicAdd(Kac, Vac[a])
34          atomicAdd(Jcd, Vcd)
35        for |a| in |a|:
36          atomicAdd(Kad, Vad[a])

```

---

Coulomb and exchange energies, respectively,  $\mathbf{W}$  is the orbital energy weighted density matrix,<sup>29</sup> and  $\mathbf{S}$  is the overlap matrix. In this work, only the computationally intensive Coulomb and exchange energy gradients are evaluated on the GPU. The contributions from the one-electron integrals are computed on the CPU (with the exception of the nuclear-electron Coulomb attraction, which is computed on the GPU using a three-center integral code that is introduced in Ref. 21), allowing for concurrent execution with the GPU calculations.

A general  $m$ -th order ERI derivative using the Rys quadrature method can be straightforwardly evaluated as follows,<sup>25</sup>

$$\nabla_{\mathbf{R}}^m \text{ERI} = \sum_n w_n \mathcal{F}_x[I_x(t_n)] \mathcal{F}_y[I_y(t_n)] \mathcal{F}_z[I_z(t_n)], \quad (11)$$

where  $\mathcal{F}$  stands for a linear function. Therefore, our GPU implementation of the nuclear gradients for the Coulomb

and exchange energies closely aligns with the implementation of `jk_kernel` described in Section III. For example, computing the nuclear gradient for the integral class (`ss|ss`) is similar to computing the energy for the integral class (`ps|ss`).

Nevertheless, the presence of the gradient operator adds an additional dimension (i.e., the nuclear coordinates  $\mathbf{R}$ ) to the ERIs. It also increases the total angular momentum by one. Moreover, while up to eight-fold permutation symmetry can be utilized in energy evaluation, at most two-fold symmetry can be exploited for the ERI gradient. Consequently, this leads to significantly higher register usage and memory footprint for evaluating the RRs and the ERI gradient. Additionally, more atomic operations are required if the Fock matrix gradient is to be computed and stored.

In order to overcome these bottlenecks, we double contract the ERI gradient with the density matrix to directly obtain the energy gradient. Specifically, this involves computing the following unique contributions on the fly:

$$\nabla_{\mathbf{R}_a} E_J = \sum_{abcd} (\nabla_{\mathbf{R}_a} ab|cd) P_{ab} P_{cd}, \quad (12)$$

$$\nabla_{\mathbf{R}_b} E_J = \sum_{abcd} (a \nabla_{\mathbf{R}_b} b|cd) P_{ab} P_{cd}, \quad (13)$$

$$\nabla_{\mathbf{R}_a} E_K = \sum_{abcd} (\nabla_{\mathbf{R}_a} ab|cd) (P_{ac} P_{bd} + P_{ad} D_{bc}), \quad (14)$$

$$\nabla_{\mathbf{R}_b} E_K = \sum_{abcd} (a \nabla_{\mathbf{R}_b} b|cd) (P_{ac} P_{bd} + P_{ad} D_{bc}). \quad (15)$$

A general implementation of the GPU kernel (`ejk_grad_kernel`) for computing  $E_J$  and  $E_K$  gradients is demonstrated in Algorithm 4 for  $N > 2$ . (Note here  $N$  is determined after applying the gradient operator to the ERIs.) Similar to Algorithm 3, the 2D integral gradients are computed once for all Rys roots and stored in local memory (line 5). However, the gradients of  $E_J$  and  $E_K$  for the two nuclear centers  $\mathbf{R}_a$  and  $\mathbf{R}_b$  comprise only 12 scalar numbers, which are cached in registers (line 1) and accumulated (lines 18–19) within the loops over the basis functions. Notably, atomic operations are no longer required within these loops. Instead, they are performed at the end of the kernel to write the results into global storage (lines 20–21), totaling 12 operations for each shell quartet. This can lead to significant performance gains compared to building the Fock matrix gradient. Finally, for  $N \leq 2$ , we cache the 2D integral gradients and other intermediates in registers to minimize memory latency.

## V. RESULTS AND DISCUSSIONS

In this section, we present the performance of our GPU-accelerated HF method, implemented within the GPU4PySCF module. All GPU calculations were performed on a single NVIDIA A100 GPU with 40 GB

---

**Algorithm 4.** `ejk_grad_kernel` for  $N > 2$

---

```

1  $J_{\alpha\chi} = K_{\alpha\chi} = 0$  # $\alpha \in \{a, b\}$   $\chi \in \{x, y, z\}$ 
2 for  $[ab]$  in  $[ab]$ :
3   for  $[cd]$  in  $[cd]$ :
4      $t, w = \text{rys\_roots} < N > ()$  #Rys roots/weights
5      $\mathbf{I}_{\alpha\chi} = \text{rr1} < N > (t, w)$  #gradient RRs
6     for  $[d]$  in  $[d]$ :
7       for  $[c]$  in  $[c]$ :
8          $P_{cd} = P_{cd}$ 
9         for  $[b]$  in  $[b]$ :
10           $P_{bc} = P_{bc}$ 
11           $P_{bd} = P_{bd}$ 
12          for  $[a]$  in  $[a]$ :
13             $PJ = P_{ab} * P_{cd}$ 
14             $PK = P_{ac} * P_{bd} + P_{ad} * P_{bc}$ 
15             $g_{\alpha\chi} = 0$ 
16            for  $i$  in range( $N$ ):
17               $g_{\alpha\chi} +=$ 
18                 $\mathcal{F}_{\alpha\chi}(\mathbf{I}_{\alpha\chi}[i]) * \mathbf{I}_{\alpha v}[i] * \mathbf{I}_{\alpha\zeta}[i]$ 
19               $J_{\alpha\chi} += g_{\alpha\chi} * PJ$ 
20               $K_{\alpha\chi} += g_{\alpha\chi} * PK$ 
21 atomicAdd( $E'_J[\alpha, \chi], J_{\alpha\chi}$ )
21 atomicAdd( $E'_K[\alpha, \chi], K_{\alpha\chi}$ )

```

---

of VRAM. For comparison, the CPU calculations were performed using the AMD EPYC 7763 CPUs with 32 threads.

First, we compare the wall times for restricted HF (RHF) energy and nuclear gradient calculations using GPU4PySCF with those of other GPU-accelerated HF codes, including GAMESS<sup>16–18</sup> and QUICK.<sup>30,31</sup> Additionally, we provide results from the multi-threaded CPU code in PySCF as a reference. The test set from Ref. 17 was used, which includes polyglycine ( $\text{Gly}_n$ ) and RNA ( $\text{RNA}_n$ ) molecules at various sizes with 213–843 atoms and 131–1155 atoms, respectively, using the STO-3G, 6-31G, and 6-31G(d) basis sets. The integral threshold  $\tau$  was set to  $10^{-10}$ .

We present the results in Table I. It is evident that GPU4PySCF outperforms QUICK in both energy and nuclear gradient calculations, achieving speedups of over a factor of two. For energy evaluations of the polyglycine systems, similar timings were observed when comparing GPU4PySCF to GAMESS. However, for the RNA systems, GAMESS outperforms GPU4PySCF, especially with the minimal basis set. Furthermore, we also compare the computational scalings for different codes in Table II. Both GPU4PySCF and QUICK exhibit approximately quadratic scaling, whereas GAMESS approaches linear scaling. Finally, GPU4PySCF is one to two orders of magnitude more efficient than PySCF, highlighting its practical usefulness.

Next, we analyze the FLOP performance of the two GPU kernels (i.e., `jk_kernel` and `ejk_grad_kernel`) for various integral classes and  $N$  values using the roofline model. Profiling was performed on a water cluster system

TABLE I. Wall times (in seconds) for 10 self-consistent field (SCF) iterations and nuclear gradient calculations for various molecules and basis sets at the RHF level of theory.

System	Basis set	$N_{\text{basis}}$	10 SCF iterations				Nuclear gradient		
			GPU4PySCF	GAMESS <sup>a</sup>	QUICK	PySCF	GPU4PySCF	QUICK	PySCF
Gly <sub>30</sub>	STO-3G	697	2.4	2.3	3.5	74.2	3.7	6.6	84.3
	6-31G	1273	6.4	15.2	12.4	238.9	7.8	18.2	288.9
	6-31G(d)	1878	17.4	34.4	44.1	477.4	29.1	61.2	579.6
Gly <sub>40</sub>	STO-3G	927	3.4	3.4	5.9	130.1	5.7	11.3	154.4
	6-31G	1693	10.4	19.2	23.0	430.1	12.4	31.1	576.6
	6-31G(d)	2498	28.9	45.9	80.2	880.7	49.7	107.0	1148.2
Gly <sub>50</sub>	STO-3G	1157	5.2	4.7	9.3	213.2	8.7	17.5	262.5
	6-31G	2113	16.0	24.3	38.0	686.8	19.8	49.2	1032.3
	6-31G(d)	3118	44.1	61.2	130.4	1444.4	74.8	168.1	2006.6
Gly <sub>60</sub>	STO-3G	1387	7.2	6.1	13.4	306.1	13.0	25.7	404.8
	6-31G	2533	21.3	31.1	57.6	1035.0	28.0	72.5	1688.3
	6-31G(d)	3738	61.2	80.8	190.9	2194.6	107.3	241.3	3278.1
Gly <sub>70</sub>	STO-3G	1617	9.4	8.0	18.5	421.7	17.3	35.8	614.5
	6-31G	2953	28.8	39.7	81.2	1439.1	37.6	101.4	2636.0
	6-31G(d)	4358	82.9	103.7	263.9	3145.9	144.3	343.8	5033.1
Gly <sub>80</sub>	STO-3G	1847	11.9	10.1	24.2	555.6	22.6	46.7	832.3
	6-31G	3373	35.9	48.4	109.0	1976.3	48.9	135.6	3959.9
	6-31G(d)	4978	107.0		352.4	4368.1	188.1	474.8	7461.2
Gly <sub>90</sub>	STO-3G	2077	15.0	12.5	31.3	713.0	28.5	58.9	1134.5
	6-31G	3793	45.0	58.5	140.7	2591.7	62.2	182.0	5750.5
	6-31G(d)	5598	134.8		554.3	5865.5	238.3	671.6	10723.6
Gly <sub>100</sub>	STO-3G	2307	18.7	14.9	39.7	908.5	40.4	75.5	1527.3
	6-31G	4213	56.3	71.4	213.1	3334.7	74.0	242.0	8093.5
	6-31G(d)	6218	172.8		668.1	7689.4	269.8	623.5	14977.0
Gly <sub>110</sub>	STO-3G	2537	21.8	17.9	49.4	1111.5	42.6	92.3	1992.5
	6-31G	4633	65.5	83.9	226.0	4217.0	92.7	283.6	11131.9
	6-31G(d)	6838	194.2		804.9	9977.5	326.5	1020.2	20468.9
Gly <sub>120</sub>	STO-3G	2767	26.0	20.8	58.5	1350.3	50.5	120.7	2569.5
	6-31G	5053	78.1		311.3	5295.4	111.0	375.4	15027.9
	6-31G(d)	7458	240.2		962.8	12702.1	427.3	1184.4	27402.3
RNA <sub>1</sub>	STO-3G	491	3.7	2.4	4.3		6.6	8.0	
	6-31G	880	13.3	21.2	18.0		16.6	23.3	
	6-31G(d)	1310	30.7	47.0	68.1		47.2	75.8	
RNA <sub>2</sub>	STO-3G	975	15.7	7.0	21.1		28.3	33.7	
	6-31G	1747	46.2	36.6	102.9		60.2	95.8	
	6-31G(d)	2602	120.4	95.8	343.7		192.8	315.4	
RNA <sub>3</sub>	STO-3G	1459	36.1	14.3	53.3		65.7	77.5	
	6-31G	2614	98.9	64.5	263.8		130.2	219.7	
	6-31G(d)	3894	318.2	184.2	880.0		508.9	717.2	
RNA <sub>4</sub>	STO-3G	1943	67.1	24.5	101.8		124.2	140.4	
	6-31G	3481	169.7	107.2	505.7		228.5	405.8	
	6-31G(d)	5186	584.7		1625.5		865.8	1328.7	
RNA <sub>5</sub>	STO-3G	2427	102.5	37.3	171.6		189.4	223.9	
	6-31G	4348	268.6	166.3	1008.2		358.5	689.2	
	6-31G(d)	6478	931.8		3162.4		1490.1	2451.7	
RNA <sub>6</sub>	STO-3G	2911	150.7	53.9	267.5		291.2	342.5	
	6-31G	5215	382.0		1454.6		514.5	1061.6	
	6-31G(d)	7770	1317.3		4612.8		2172.0	3655.8	
RNA <sub>7</sub>	STO-3G	3395	206.7	71.2	374.9		358.8	485.1	
	6-31G	6082	509.8		2050.0		659.2	1430.6	
	6-31G(d)	9062	1790.7		6258.1		2735.3	4680.6	
RNA <sub>8</sub>	STO-3G	3879	283.0	97.2	480.2		515.8	683.8	
	6-31G	6949	702.2		2845.2		893.2	2025.6	
	6-31G(d)	10354	2513.8		8953.9		3793.4	7149.2	
RNA <sub>9</sub>	STO-3G	4363	344.5	118.3	647.8		679.0	855.5	
	6-31G	7816	837.0		3560.8		1163.6	2485.7	
	6-31G(d)	11646	3008.3		11095.9		4624.3	8687.9	

<sup>a</sup> Results are obtained from Ref. 17.

TABLE II. Observed computational scalings [ $a$  in  $O(N_{\text{basis}}^a)$ ] for energy and nuclear gradient calculations using different RHF codes.

system	basis set	10 SCF iterations				Nuclear Gradient		
		GPU4PySCF	GAMESS	QUICK	PySCF	GPU4PySCF	QUICK	PySCF
Gly <sub>x</sub>	STO-3G	1.77	1.62	2.07	2.16	1.96	2.08	2.49
	6-31G	1.81	1.35	2.32	2.29	1.94	2.20	2.88
	6-31G(d)	1.91	1.31	2.28	2.42	1.91	2.15	2.81
RNA <sub>x</sub>	STO-3G	2.08	1.81	2.29		2.10	2.14	
	6-31G	1.91	1.28	2.43		1.94	2.16	
	6-31G(d)	2.12	1.23	2.35		2.12	2.19	

consisting of 32 water molecules, using the cc-pVTZ basis set, which includes up to  $f$  functions. The results are displayed in Figs. 1 and 2, respectively.

The roofline (solid blue line) represents the performance bound of the NVIDIA A100 GPU, which includes a ceiling derived from the peak memory bandwidth (diagonal line) and the processor’s peak FLOP rate (horizontal line). The dashed black line indicates the machine balance (6.1FLOP/byte). Kernels with arithmetic intensity smaller than the machine balance are considered memory-bound, while those with arithmetic intensity greater than it are compute-bound.

From Fig. 1, we observe that for most integral classes with  $N \leq 3$  [e.g., (ss|ss), (ps|ss), (ds|ss), and (pp|pp)], `jk_kernel` is compute-bound and achieves an impressive FLOP rate ranging from 2TFLOP/s to 5TFLOP/s. However, there are exceptions, such as the integral class (dp|pp), which exhibits a memory-bound character and limited FLOP performance. This is due to the need for caching more than 234 FP64 words for intermediates per GPU thread, which exceeds the maximum number of registers (255 FP32 words) each thread can use by nearly a factor of two. Consequently, intermediates that cannot fit into registers are likely stored in slow memory (known as register spilling), resulting in significant memory latency when accessed frequently.

For  $N > 3$ , `jk_kernel` is always memory-bound due to the use of local memory for storing intermediates. Nonetheless, the kernel generally utilizes the GPU hardware efficiently, as indicated by data points lying close to the roofline. An exception is the integral class (ff|ff) (with  $N = 7$ ), which shows a potential loss of parallelization. This is mainly because of the insufficient workload to fully occupy the streaming multiprocessors (SMs), as only O atoms contain  $f$  shells, and each O atom contains only one shell of  $f$  functions.

Similarly, `ejk_grad_kernel` shows a remarkable FLOP performance of over 3TFLOP/s for integral classes with  $N \leq 2$ , where intermediates can be cached in registers. For  $N > 2$ , the kernel is again memory-bound due to the use of local memory. However, all data points in Fig. 2 lie close to the roofline, indicating efficient utilization of the GPU hardware. Notably, even for  $N = 7$ , a FLOP rate of 0.8TFLOP/s is achieved, outperforming

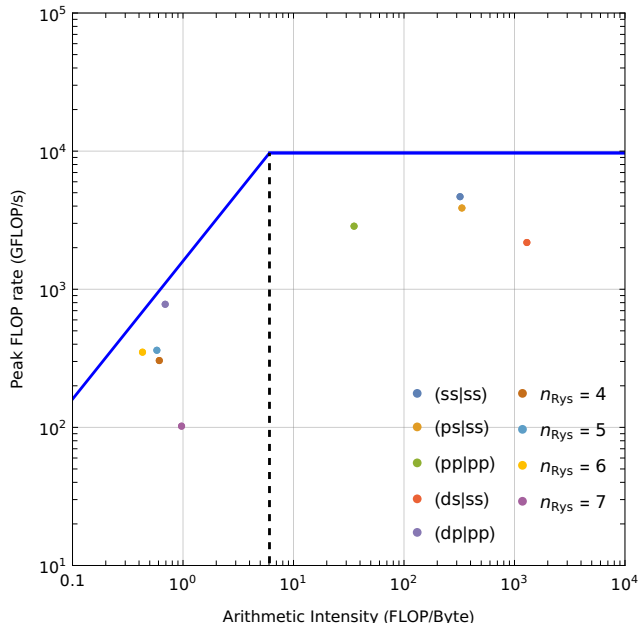


FIG. 1. FLOP performance of the GPU kernels `jk_kernel` analyzed using the roofline model on the NVIDIA A100 GPU. The solid blue line represents the official peak FP64 FLOP rate of 9.7TFLOP/s (horizontal) and peak memory bandwidth of 1.6TB/s (diagonal). The dashed black line indicates the machine balance of 6.1FLOP/byte. The calculations were performed for a water cluster system consisting of 32 water molecules at the RHF/cc-pVTZ level of theory.

its `jk_kernel` counterpart for Fock builds by a factor of eight. This can be attributed to our integral direct approach as shown in Algorithm 4. It eliminates the need to compute the Fock matrix gradient, which would otherwise be stored in global memory. As a result, significantly fewer atomic operations and slow memory accesses are performed, enhancing cache utilization. In addition, the workload involved in gradient calculations is greater than that in Fock builds [e.g., the integral class (ff|fd) also corresponds to  $N = 7$  when evaluating its gradient], which keeps more GPU threads active and helps hide latency more effectively.

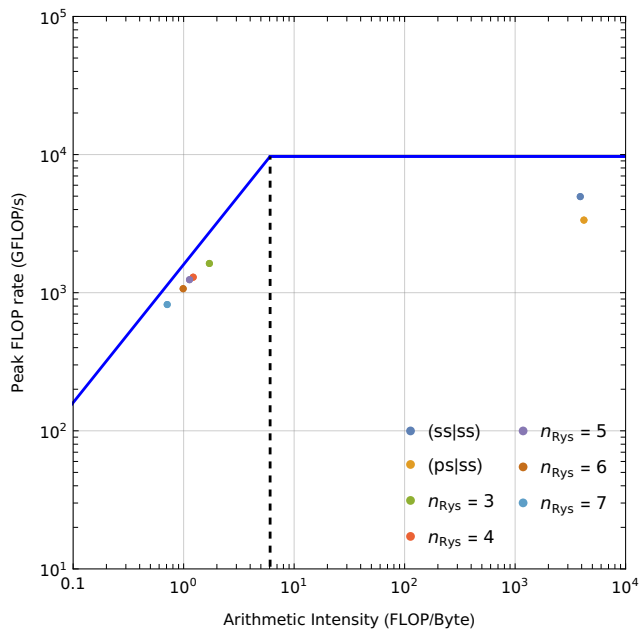


FIG. 2. Same as Fig. 1, but for the GPU kernels `ejk_grad_kernel`.

## VI. CONCLUSIONS

In this work, we introduced the GPU4PySCF module, and in particular, the core ERI CUDA kernels that form the starting point for accelerating quantum chemistry calculations. As an example of their use, we described a GPU-accelerated HF method for energy and nuclear gradient calculations, including the detailed optimizations required to achieve high GPU efficiency.

The GPU acceleration of quantum chemistry is integral not only to advancing traditional quantum chemistry calculations, but also to bringing quantum chemical methods and data into new disciplines such as machine learning. We hope that by providing a community-based, open-source implementation of GPU accelerated quantum chemistry algorithms, we can help the growth of quantum chemistry in these areas. Indeed, we note that as a living open-source code, at the time of writing GPU4PySCF already contains new contributions targeted at these directions.<sup>21</sup>

## ACKNOWLEDGEMENTS

We acknowledge the generous contributions of the open-source community to the GPU4PySCF module. RL and QS contributed equally to this work. Work carried out by QS (development of initial ERI code and Fock build) was performed as a part of a software contract with GKC through the California Institute of Technology, funded by internal funds. RL (development of gradient ERIs and gradient code) and GKC (project super-

vision) were supported by the US Department of Energy, Office of Science, through Award No. DE-SC0023318. XZ (additional data analysis) was supported by the Center for Molecular Magnetic Quantum Materials, an Energy Frontier Research Center funded by the U.S. Department of Energy, Office of Science, Basic Energy Sciences under Award No. DE-SC0019330. This research used resources of the National Energy Research Scientific Computing Center (NERSC), a U.S. Department of Energy Office of Science User Facility located at Lawrence Berkeley National Laboratory, operated under Contract No. DE-AC02-05CH11231 using NERSC award ERCAP-0024087.

## REFERENCES

- A. Paszke, S. Gross, F. Massa, A. Lerer, J. Bradbury, G. Chanan, T. Killeen, Z. Lin, N. Gimelshein, L. Antiga, A. Desmaison, A. Kopf, E. Yang, Z. DeVito, M. Raison, A. Tejani, S. Chilamkurthy, B. Steiner, L. Fang, J. Bai, and S. Chintala, “Pytorch: An imperative style, high-performance deep learning library,” in *Advances in Neural Information Processing Systems 32* (Curran Associates, Inc., 2019) pp. 8024–8035.
- M. Abadi, A. Agarwal, P. Barham, E. Brevdo, Z. Chen, C. Citro, G. S. Corrado, A. Davis, J. Dean, M. Devin, S. Ghemawat, I. Goodfellow, A. Harp, G. Irving, M. Isard, Y. Jia, R. Jozefowicz, L. Kaiser, M. Kudlur, J. Levenberg, D. Mane, R. Monga, S. Moore, D. Murray, C. Olah, M. Schuster, J. Shlens, B. Steiner, I. Sutskever, K. Talwar, P. Tucker, V. Vanhoucke, V. Vasudevan, F. Viegas, O. Vinyals, P. Warden, M. Wattenberg, M. Wicke, Y. Yu, and X. Zheng, “Tensorflow: Large-scale machine learning on heterogeneous distributed systems,” (2016), arXiv:1603.04467 [cs.DC].
- P. Springer and C.-H. Yu, “cutensor: High-performance cuda tensor primitives,” in *NVIDIA GPU Technology Conference 2019* (2019).
- “Nersc perlmuter architecture,” <https://docs.nersc.gov/systems/perlmuter/architecture/>.
- K. Yasuda, “Two-electron integral evaluation on the graphics processor unit,” *Journal of Computational Chemistry* **29**, 334 (2008).
- C. A. White and M. Head-Gordon, “Aj matrix engine for density functional theory calculations,” *The Journal of chemical physics* **104**, 2620–2629 (1996).
- M. Challacombe and E. Schwegler, “Linear scaling computation of the fock matrix,” *The Journal of chemical physics* **106**, 5526–5536 (1997).
- I. S. Ufimtsev and T. J. Martínez, “Quantum chemistry on graphical processing units. 1. strategies for two-electron integral evaluation,” *Journal of Chemical Theory and Computation* **4**, 222 (2008).
- I. S. Ufimtsev and T. J. Martínez, “Quantum chemistry on graphical processing units. 2. direct self-consistent-field implementation,” *Journal of Chemical Theory and Computation* **5**, 1004 (2009).
- L. E. McMurchie and E. R. Davidson, “One- and two-electron integrals over cartesian gaussian functions,” *Journal of Computational Physics* **26**, 218–231 (1978).
- A. Asadchev, V. Allada, J. Felder, B. M. Bode, M. S. Gordon, and T. L. Windus, “Uncontracted rys quadrature implementation of up to g functions on graphical processing units,” *Journal of Chemical Theory and Computation* **6**, 696–704 (2010).
- M. Dupuis, J. Rys, and H. F. King, “Evaluation of molecular integrals over gaussian basis functions,” *The Journal of Chemical Physics* **65**, 111–116 (1976).



- <sup>13</sup>J. Rys, M. Dupuis, and H. F. King, "Computation of electron repulsion integrals using the rys quadrature method," *Journal of Computational Chemistry* **4**, 154–157 (1983).
- <sup>14</sup>Y. Miao and K. M. J. Merz, "Acceleration of electron repulsion integral evaluation on graphics processing units via use of recurrence relations," *Journal of Chemical Theory and Computation* **9**, 965–976 (2013).
- <sup>15</sup>M. Head-Gordon and J. A. Pople, "A method for two-electron gaussian integral and integral derivative evaluation using recurrence relations," *The Journal of Chemical Physics* **89**, 5777–5786 (1988).
- <sup>16</sup>G. M. J. Barca, J. L. Galvez-Vallejo, D. L. Poole, A. P. Rendell, and M. S. Gordon, "High-performance, graphics processing unit-accelerated fock build algorithm," *Journal of Chemical Theory and Computation* **16**, 7232–7238 (2020).
- <sup>17</sup>G. M. J. Barca, M. Alkan, J. L. Galvez-Vallejo, D. L. Poole, A. P. Rendell, and M. S. Gordon, "Faster self-consistent field (scf) calculations on gpu clusters," *Journal of Chemical Theory and Computation* **17**, 7486–7503 (2021).
- <sup>18</sup>F. Zahariev, P. Xu, B. M. Westheimer, S. Webb, J. Galvez Vallejo, A. Tiwari, V. Sundriyal, M. Sosonkina, J. Shen, G. Schoendorff, M. Schlinsog, T. Sattasathuchana, K. Ruedenberg, L. B. Roskop, A. P. Rendell, D. Poole, P. Piecuch, B. Q. Pham, V. Mironov, J. Mato, S. Leonard, S. S. Leang, J. Ivanic, J. Hayes, T. Harville, K. Gururangan, E. Guidez, I. S. Gerasimov, C. Friedl, K. N. Ferreras, G. Elliott, D. Datta, D. D. A. Cruz, L. Carrington, C. Bertoni, G. M. J. Barca, M. Alkan, and M. S. Gordon, "The general atomic and molecular electronic structure system (gamess): Novel methods on novel architectures," *Journal of Chemical Theory and Computation* **19**, 7031–7055 (2023).
- <sup>19</sup>A. Asadchev and E. F. Valeev, "High-performance evaluation of high angular momentum 4-center gaussian integrals on modern accelerated processors," *The Journal of Physical Chemistry A* **127**, 10889–10895 (2023).
- <sup>20</sup>A. Asadchev and E. F. Valeev, "3-center and 4-center 2-particle gaussian ao integrals on modern accelerated processors," (2024), arXiv:2405.01834 [physics.comp-ph].
- <sup>21</sup>X. Wu, Q. Sun, Z. Pu, T. Zheng, W. Ma, W. Yan, X. Yu, Z. Wu, M. Huo, X. Li, W. Ren, S. Gong, Y. Zhang, and W. Gao, "Python-based quantum chemistry calculations with gpu acceleration," (2024), arXiv:2404.09452 [physics.comp-ph].
- <sup>22</sup>C. R. Harris, K. J. Millman, S. J. van der Walt, R. Gommers, P. Virtanen, D. Cournapeau, E. Wieser, J. Taylor, S. Berg, N. J. Smith, R. Kern, M. Picus, S. Hoyer, M. H. van Kerkwijk, M. Brett, A. Haldane, J. F. del Río, M. Wiebe, P. Peterson, P. Gérard-Marchant, K. Sheppard, T. Reddy, W. Weckesser, H. Abbasi, C. Gohlke, and T. E. Oliphant, "Array programming with NumPy," *Nature* **585**, 357–362 (2020).
- <sup>23</sup>R. Okuta, Y. Unno, D. Nishino, S. Hido, and C. Loomis, "Cupy: A numpy-compatible library for nvidia gpu calculations," in *Proceedings of Workshop on Machine Learning Systems (LearningSys) in The Thirty-first Annual Conference on Neural Information Processing Systems (NIPS)* (2017).
- <sup>24</sup>Q. Sun, X. Zhang, S. Banerjee, P. Bao, M. Barbry, N. S. Blunt, N. A. Bogdanov, G. H. Booth, J. Chen, Z.-H. Cui, J. J. Eriksen, Y. Gao, S. Guo, J. Hermann, M. R. Hermes, K. Koh, P. Koval, S. Lehtola, Z. Li, J. Liu, N. Mardirossian, J. D. McClain, M. Motta, B. Mussard, H. Q. Pham, A. Pulkin, W. Purwanto, P. J. Robinson, E. Ronca, E. R. Sayfutyarova, M. Scheurer, H. F. Schurkus, J. E. T. Smith, C. Sun, S.-N. Sun, S. Upadhyay, L. K. Wagner, X. Wang, A. White, J. D. Whitfield, M. J. Williamson, S. Wouters, J. Yang, J. M. Yu, T. Zhu, T. C. Berkelbach, S. Sharma, A. Y. Sokolov, and G. K.-L. Chan, "Recent developments in the pyscf program package," *The Journal of Chemical Physics* **153**, 024109 (2020).
- <sup>25</sup>N. Flocke and V. Lotrich, "Efficient electronic integrals and their generalized derivatives for object oriented implementations of electronic structure calculations," *Journal of Computational Chemistry* **29**, 2722–2736 (2008).
- <sup>26</sup>S. Williams, A. Waterman, and D. Patterson, "Roofline: an insightful visual performance model for multicore architectures," *Communications of the ACM* **52**, 65–76 (2009).
- <sup>27</sup>Q. Sun, "Libcint: An efficient general integral library for gaussian basis functions," *Journal of Computational Chemistry* **36**, 1664–1671 (2015).
- <sup>28</sup>J. L. Whitten, "Coulombic potential energy integrals and approximations," *The Journal of Chemical Physics* **58**, 4496–4501 (1973).
- <sup>29</sup>J. A. Pople, R. Krishnan, H. B. Schlegel, and J. S. Binkley, "Derivative studies in hartree-fock and møller-plesset theories," *International Journal of Quantum Chemistry* **16**, 225–241 (1979).
- <sup>30</sup>M. Manathunga, A. Shajan, J. Smith, Y. Miao, X. He, K. Ayers, E. Brothers, A. W. Götz, and K. M. Merz, "Quick-23.08," University of California San Diego, CA and Michigan State University, East Lansing, MI (2023).
- <sup>31</sup>M. Manathunga, Y. Miao, D. Mu, A. W. Götz, and K. M. J. Merz, "Parallel implementation of density functional theory methods in the quantum interaction computational kernel program," *Journal of Chemical Theory and Computation* **16**, 4315–4326 (2020).